

We are IntechOpen, the world's leading publisher of Open Access books Built by scientists, for scientists

6,300

Open access books available

172,000

International authors and editors

190M

Downloads

Our authors are among the

154

Countries delivered to

TOP 1%

most cited scientists

12.2%

Contributors from top 500 universities



WEB OF SCIENCE™

Selection of our books indexed in the Book Citation Index
in Web of Science™ Core Collection (BKCI)

Interested in publishing with us?
Contact book.department@intechopen.com

Numbers displayed above are based on latest data collected.
For more information visit www.intechopen.com



Chapter

Hierarchical Control of an Islanded AC Micro Grid Using FS-MPC and an EMS

Andreas Pedersen, Ibrahim Ahmed and Lucian Mihet-Popa

Abstract

Microgrids and distributed energy resources (DERs) are gaining popularity owing to their efficient operation, autonomy, and dependability. Microgrids provide several new opportunities, one of which is the ability to deliver electricity continuously, even in the event of a grid failure. This chapter will first describe the modeling of DER components in a microgrid, with each component using Finite Set-Model Predictive Control (FS-MPC) for controlling the inverters to be robust, to have a fast response, to account for multiple objectives, and to eliminate manual tuning. In addition, droop control will be used to provide a voltage reference for the FS-MPC. The PV-inverter will operate as a grid-forming inverter, while the other inverters will serve as grid-feeding inverters. The proposed inverter models are validated using simulations. The microgrid has been modeled using MATLAB-Simulink software package. A supervisory controller for energy management system of the microgrid to operate in different power flows through the proposed control algorithm has also been designed. The simulation results show the effectiveness and robustness of the proposed controller during dynamic performance and transients, and the developed energy management system algorithm successfully controlled the power flow to ensure continuous power delivery to the load under all circumstances.

Keywords: AC microgrid (MG), droop control, finite-set model predictive control (FS-MPC), hierarchical control, islanded operation, energy management system (EMS), energy storage systems (ESSs)

1. Introduction

Today's society needs a dependable supply of electricity to consumers and prosumers, with high power quality. As a result of the continual adoption of novel technologies, the structure of the power grid in many countries is continuously developing, posing difficulties with energy flow changes, capacity limits, and high investment expenditures to update the power grid. For many years, power grids have been digitalized to allow centralized monitoring and administration of the power network, which is a result of the emergence of new technologies [1–6]. This “smart” digitalized grid has been a reality for the high-voltage section of the power system for a

considerable amount of time, and the modernization of the low-voltage distribution sector is also in progress [7–9]. In the next years, utility grids will depend more and more on renewable energy, and users will reap the benefits of smart technologies such as electric car chargers and smart meters [10–13].

This gives an opportunity to further digitize the distribution (low-voltage) sector of the grid. One method to do this is by establishing a microgrid. In the event of maintenance or grid failure, microgrids should be able to function independently of the utility grid [14].

Hierarchical control structures consist of a primary control layer that has a quick response in milliseconds, a secondary control layer that is used to reduce steady-state errors and acts in a couple of seconds, and finally, a tertiary control layer that controls the active and reactive energy flow within the microgrid by sending power references either manually by the grid operator or automatically by an Energy Management System (EMS) that balances the net power within the microgrid [1–3].

Due to the intermittent nature of RES, it is required to incorporate a backup power source such as a battery storage system, and perhaps an additional fuel-based power source, so that the microgrid may continue to run even if the battery is depleted or the maximum discharge current is reached [15–17].

The authors in [18] proposed a MPC strategy developed in Python to optimize energy production and load management for interactive buildings integrated PV & BESS (battery energy storage system). The forecasting method used in the study involves Weighted Moving Average (WMA) combined with Trigg's tracking signal and adjustment formulas. This method includes sensitivity parameters and thresholds that allow a stricter or looser approach to be taken in forecasting time series. The proposed method adjusts the forecasted values for the rest of the planning horizon based on the deviation detected between forecasted and real-time series. The adjustment formula of a building's PV production is different from the adjustment formula of its load since the production of PV is more predictable than the load of a building, especially when it comes to residential loads.

In these research papers [19–22] the performance of the MPC design procedure for DC-DC and DC-AC converters applied to a PV system was analyzed. The authors in [19] presented a continuous control set MPC designed for a DC-DC buck converter used in a MPPT of a PV module, while in [20] an adaptive MPC for current sensorless MPPT in PV systems was evaluated. The papers [21, 22] address the optimal control problems of a grid-connected PV inverter system MPC-based MPPT method. The steady-state and dynamic performance of the MPC-based system are verified and compared with traditional controllers.

Furthermore, authors in [23] presented an examination of a predictive control method designed to prevent imbalances between the load demand and the generation capacity in an islanded microgrid. The Nonlinear Model Predictive Control (NMPC) is utilized to calculate load shedding and manage energy from batteries within an optimization framework. This results in the establishment of an optimal control problem that integrates all the microgrid's operating conditions, including load priorities for disconnection, and charging and discharging cycles of batteries. Simulation results of the microgrid's performance with and without the Microgrid Central Controller (MGCC) were compared. The results demonstrate that the control strategy can improve the reliability of the microgrid when operating in islanded mode, as the control strategy can maintain the voltage and frequency of the microgrid within safe limits and achieve a correct balance between generated power and load demand.

The motivation to carry out this study is the growing interest of RES based DG units & ESSs. This chapter is focused on modeling and simulation of an AC microgrid, developed in MATLAB-Simulink environment, which consists of a hydrogen fuel cell, a solar farm, a wind turbine, and a utility grid [24–32]. Verification by simulations with a hierarchical control structure to operate the AC microgrid in islanded mode has been performed. The primary control mainly consists of FS-MPC, where the solar farm inverter is modeled as a grid-forming inverter [29, 30, 33], and FS-MPC, which was modeled as described in [34–38], is shown to be highly robust in a variety of different scenarios. The EMS is created to protect the battery' SOC, and the maximum charging/discharging current from being reached while keeping the power balance stable in the microgrid. The constraints of operating the AC microgrid in islanded operation are the maximum discharging off the battery and fuel cell, and the stochastic RES. The novelty of this research chapter is the use of FS-MPC in the primary control with a new EMS algorithm that is highly robust during islanded operation.

The main contributions of this chapter can be summarized as follows:

1. Modeling and simulation of DER components in an AC Microgrid, including the primary and secondary controllers.
2. The primary controllers are designed to be robust and resilient based on finite-set model predictive control, which is capable of handling sudden changes in the load demand.
3. An algorithm for EMS is developed for managing the energy flow if the microgrid is completely detached from the grid and operating in islanded mode.
4. Various scenarios are developed to test and prove the robustness of the controllers.

The chapter is organized as follows. Section 2 describes the modeling of DER components in the AC microgrid, including the design of the LCL grid inverter filter, while in Section 3 the proposed EMS strategy is described and validated by simulations, using many different scenarios. The conclusion section summarizes the main outcomes of the paper.

2. Modeling of DER components

This section describes how we created and developed detailed models for many microgrid components that make up the proposed microgrid. In the following sections, each component, including equations, parameters, and other design factors, will be thoroughly examined. The MATLAB-Simulink software program is used to implement all simulation models. The various component models are well-known and available in the literature, however the parameters, filter designs, and converter designs have been adjusted and chosen to match the requirements of the proposed microgrid model.

The general structure of the proposed microgrid is displayed in **Figure 1**. A solar farm, a wind turbine, a lithium-ion battery, a hydrogen fuel cell, and a utility grid are all part of the proposed AC microgrid. The AC microgrid (MG) architecture has been chosen instead of a DC architecture owing to its compatibility with existing

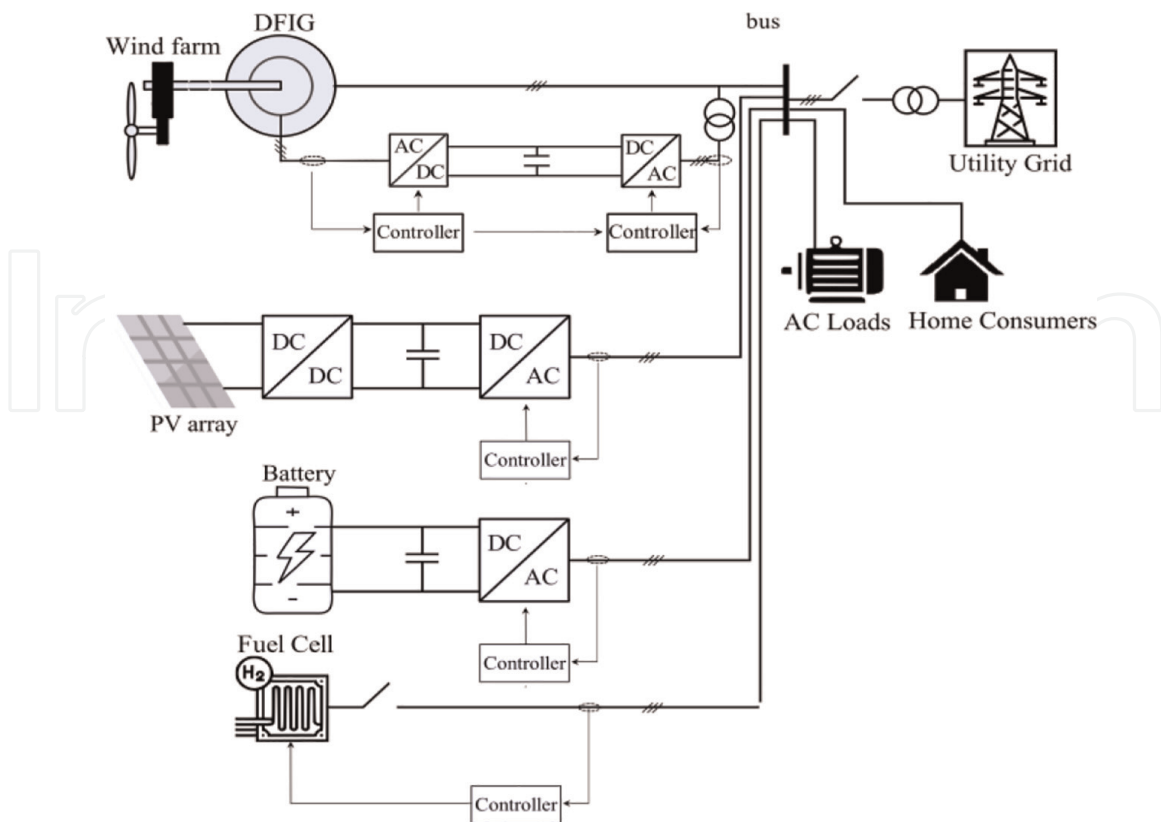


Figure 1.
General structure of the proposed microgrid.

infrastructure and greater flexibility in power distribution network. AC MGs are emerging and becoming more attractive structures with integration of RES based DG units and ESSs in order to manage our future energy demands based flexibility, digitalization and energy transition, but also as a viable and reliable solution to the population without access to energy or with poor energy supply to effectively reduce the greenhouse gas emissions. The microgrid requires a battery to handle electrical loads during periods of low renewable energy generation because renewable energy supply is highly variable and depends on the environmental conditions. The microgrid may be confronted with extended periods of low irradiance and low wind speed, potentially resulting in a fully discharged battery. In this instance, if the utility grid is unavailable, a hydrogen-fueled fuel cell can be employed to meet the load demand.

2.1 PV system

Multiple photovoltaic arrays with a combined capacity of 60 kW make up the solar farm. A boost converter is used to boost the DC output of the photovoltaic arrays and keep the PV modules' generation at its highest level. A three-phase full-bridge inverter is employed because the microgrid's PCC is a three-phase AC system, and the three-phase square waves from the inverter are subsequently filtered using an LCL filter.

Figure 2 illustrates the model [39].

2.1.1 Photovoltaic array

The MATLAB-Simulink special power system library provides the photovoltaic array model/block/subsystem, which we have utilized in the microgrid simulation.

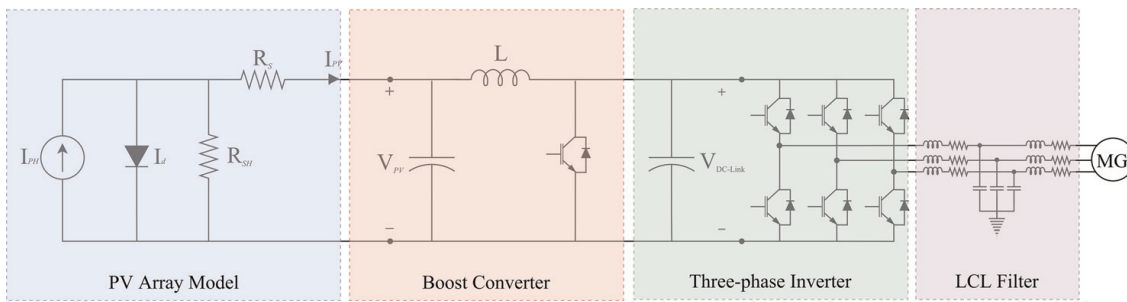


Figure 2.
 Model of the PV system [39].

It is a five-parameter single-diode model that uses a light-generated current source (I_{ph}) and a diode current (I_d) to simulate an ideal PV cell with a series resistance (R_s) and a parallel-coupled shunt resistance (R_{sh}) to simulate a more practical solar cell and more accurately describes the solar cells' power losses. The one-diode model is one of the most popular models because of the good compromise between simplicity and precision [7, 24, 33, 37–39].

The I-V characteristic of the solar cell can then be derived by using the single-exponential Shockley equation for the diode, and the resistances to get Eq. (1) [33].

$$I = I_{ph} - I_0 \left(e^{\frac{V+R_s I}{nV_t}} - 1 \right) - \left(\frac{V + R_s I}{R_{sh}} \right) \quad (1)$$

where I_0 is the reverse saturation current, n is the ideality factor of the diode, and V_t is the thermal voltage. Eq. (2) describes the light-generated current I_{ph} which is based on the value of irradiance (G), the cell temperature (T_c), the STC (Standard Test Condition) of the irradiance (G_{ref}), and cell temperature (T_{ref}), the temperature coefficient k_i ($A/^\circ C$), and the short-circuit current at STC (I_{sc}) [29].

The reverse saturation current is given by Eq. (2), where the I_{sc} is the short-circuit current, V_{oc} is the open-circuit voltage, V_{to} is the STC thermal voltage, E_g is the energy bandgap of the semiconductor, and the energy bandgap at $T = 0$ K (E_{go}) [29].

$$I_0 = \frac{I_{SC} e^{\left(\frac{E_{go}}{V_{to}} - \frac{E_g}{V_t} \right)}}{e^{\left(\frac{V_{OC}}{nN_s V_{to}} \right)} - 1} \cdot \left(\frac{T_C}{T_{ref}} \right)^3 \quad (2)$$

Next, the semiconductors energy bandgap value at any cell temperature (T_c) is described by Eq. (3), where the α_{gap} , and β_{gap} are the characteristic parameters of the semiconductor [33, 35].

$$E_g = E_{go} - \frac{\alpha_{gap} T_C^2}{\beta_{gap} + T_C} \quad (3)$$

However, several solar cells are connected in series in a photovoltaic module, and some modules may have multiple parallel branches of the series connections. The solar cell equations can be scaled up by representing the number of solar cells connected in series as (N_s) and the number of parallel branches (N_p). The scaling is performed on

the module current ($I_m = N_p I$), module voltage ($V_m = N_s V$), module series resistance ($R_{sm} = \frac{N_s}{N_p} R_s$) and module shunt resistance ($R_{shm} = \frac{N_s}{N_p} R_{sh}$) [29, 32].

Furthermore, by denoting the number of PV modules connected in series by (N_{sm}) and the number of series strings connected in parallel by (N_{pm}), the PV modules can be scaled up to create a PV array.

The MPP (Maximum Power Point) of the PV array current (I_{mg}) and PV array voltage (V_{mg}) can therefore be characterized using the Eqs. (4) and (5), respectively [33].

$$I_{mg} = N_{pm} \left(\frac{I_{mm} R}{1000} G + \left(\frac{dI_{scm}}{dT} \right) (T_c - T_{ref}) \right) \quad (4)$$

$$V_{mg} = N_{sm} \left(N_s V_t \ln \left(1 + \frac{I_{scm} - I_{mg}}{I_{scm}} \left(e^{\frac{V_{ocm}}{N_s V_t}} - 1 \right) \right) - I_{mg} R_{sm} \right) \quad (5)$$

Where I_{mmg} is the rated MPP current of the module at STC, I_{scm} is the short-circuit current of the module at STC, V_{ocm} is the open-circuit voltage of the module at STC. The PV- module operating temperature (T_c), can then be found for any irradiance condition, and ambient air temperature (T_{air}), as shown in Eq. (6). NOCT is the normal operating cell temperature at an irradiance of 800 W/m^2 , and an ambient air temperature of 20°C [33].

$$T_c = T_{air} + \frac{NOCT - 20}{800} G \quad (6)$$

It is worth noting that the single-diode model has poor accuracy for extremely low irradiances, but the two-diode model can be utilized to improve accuracy in these cases. The two-diode model, on the other hand, is substantially slower to simulate because it has seven parameters and two exponential components, and the accuracy at low irradiances has no effect on the overall output power.

2.1.2 Boost converter and MPPT

The boost converter is a DC/DC converter that increases the output voltage through active switching. The boost converter contains an input capacitor, an inductor, an IGBT, a diode, and an output capacitor and is built using blocks from the MATLAB-Simulink special power system library. **Figure 3** shows the MATLAB-Simulink model.

When the gate of the IGBT receives a square wave of sufficient magnitude, it conducts (ON state), creating a short circuit between the inductor and the negative input. The inductor on the input side stores energy in the magnetic field, and the current will only pass through the IGBT because the diode, capacitor, and load all have much greater impedances.

There is no path through the IGBT when it is turned off, and the abrupt drop in current causes the inductor to generate a back EMF with the polarity of the voltage across it during the ON period. As a result, two voltages are generated, one from the supply and the other from the inductor. The current going through the diode is now charging the capacitor and powering the load at the same time. Even if no current passes from the input to the output during the ensuing on-period, the output capacitor will retain charge and continue to power the load [7].

Because the output voltage remains constant in a steady state, the integral of the inductor voltage over one period is zero. Eq. (7) can therefore be used to explain the

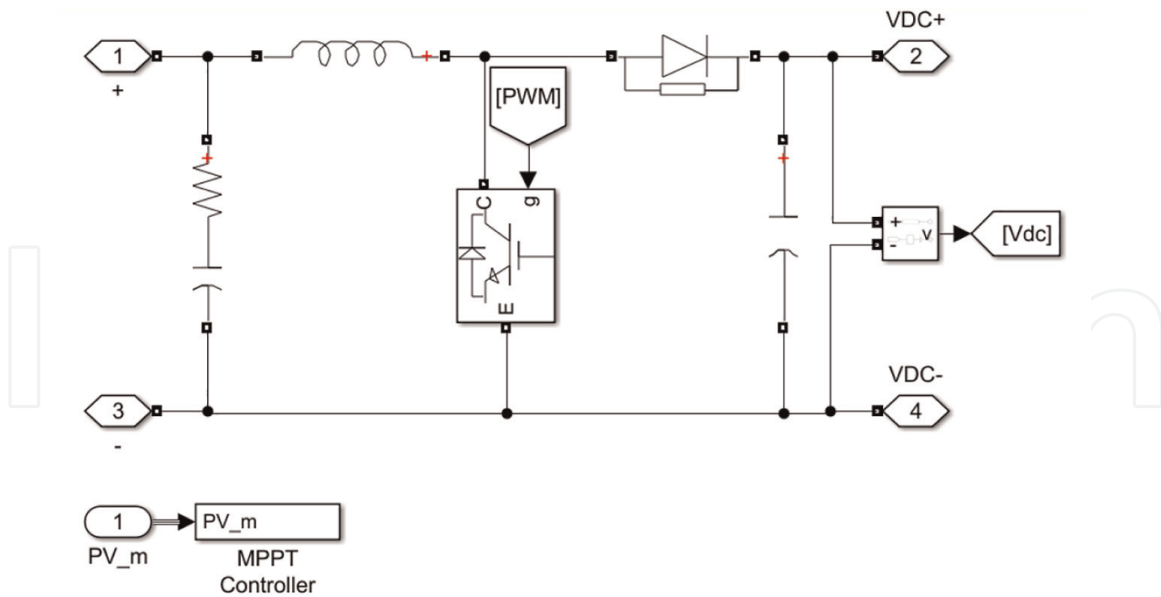


Figure 3. MATLAB-Simulink model of the boost converter modeled with blocks from Simscape/SPS library and the MPPT controller based on a MATLAB function.

dynamics in CCM (Continuous Conduction Mode). After that, divide both sides of Eq. (7) with

T_s and rearrange to get Eq. (8) [7].

$$V_i t_{on} + (V_i - V_o) t_{off} = 0 \quad (7)$$

$$\frac{V_o}{V_i} = \frac{T_s}{t_{off}} = \frac{1}{1 - D} \quad (8)$$

Where V_i is the input voltage, V_o is the average output voltage, t_{on} , and t_{off} are the time the IGBT is switched on, and off during one period respectively, T_s is the switching period, and D is the duty cycle.

We can define the minimal amount of inductance required to function at CCM when choosing the inductor. Eq. (10) may be used to compute the critical inductance value, whereas Eq. (9) can be used to calculate the duty cycle [7].

$$D = 1 - \frac{V_{mpp}}{V_{o-nom}} \quad (9)$$

$$L_c = \frac{V_{mpp} D}{\Delta I_L f_{sw}} \quad (10)$$

Where V_{mpp} is the PV-maximum array's rated voltage at maximum irradiance and lowest ambient temperature. The nominal output voltage is V_{oNom} , the inductor ripple current is ΔI_L , and the switching frequency is f_{sw} . Eqs. (11) and (12) may then be used to compute the capacitance required at the input and output [7].

$$C_{in} = \frac{\Delta I_L}{8 \Delta V_{pv} f_{sw}} \quad (11)$$

$$C_{out} \geq \frac{V_o D}{f_{sw} \Delta V_o R} \quad (12)$$

2.1.3 MPPT algorithm

To always generate the maximum possible power with the PV array, an MPPT (Maximum Power Point Tracking) algorithm is used [37]. The algorithm that is used in this simulation is called P&O (Perturb & Observe) and its flowchart is visualized in **Figure 4**. The MPPT generates a voltage reference in the model. The duty cycle for the PWM generation is then produced by feeding the difference between the observed voltage and the voltage reference into a PI controller.

2.1.4 Three-phase square-wave inverter

The three-phase full-bridge inverter is a switching transistor-based DC/AC converter. A large-value capacitor is utilized in the DC-link to smooth out the input voltage to the inverter since VSIs (Voltage Source Inverters) depend on a consistent DC source. The square-formed sine wave that the inverter outputs as AC voltage must first be filtered before reaching the PCC [38, 40, 41].

The six IGBTs that make up the three-phase, two-level inverter are split into three at the top that are connected to one of the phase outputs from the positive DC input and three more that are connected to the same output from the negative DC input. To

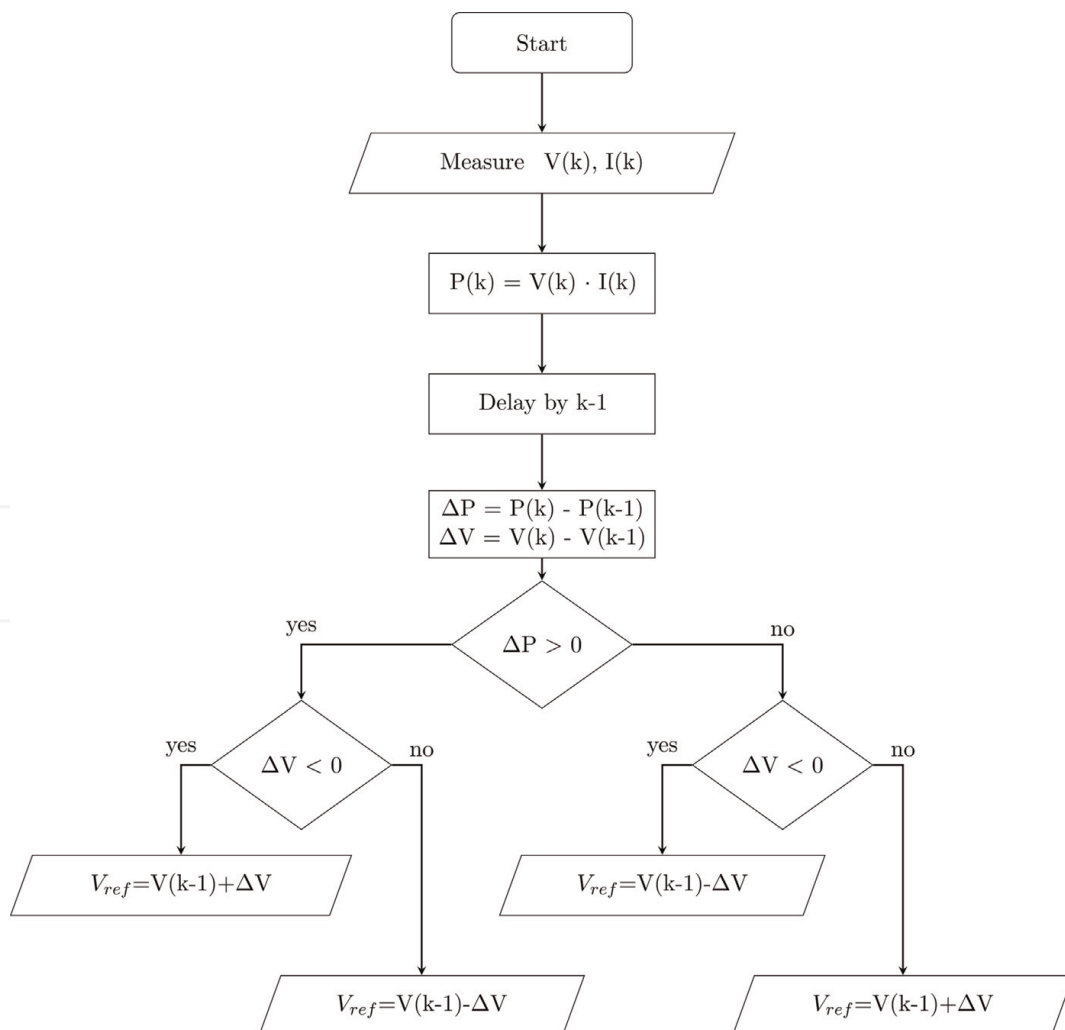


Figure 4. MATLAB-Simulink MPPT algorithm used for controlling the duty cycle of the boost converter.

prevent a short circuit, it is crucial that never both of an IGBT's top and bottom levels conduct at once. **Figures 5** and **6** show the three-phase square wave inverter's basic setup and the voltage for each phase, respectively.

2.1.5 LCL filter

For applications that employ a VSI, a filter is necessary to improve the performance of the feedback control and reduce harmonics. There are many different filters that can be utilized, but in this instance an LCL filter is used [27, 28, 37, 38]. The LCL filter offers greater attenuation than using a single high-value inductor. Even at power levels of hundreds of kW, the capacitor and inductor values might be minimal. The current ripple, filter size, and switching ripple attenuation must all be considered while creating an LCL filter for a VSI. Additionally, both the inductor and the capacitor may contribute if the controller is used to regulate reactive power, necessitating

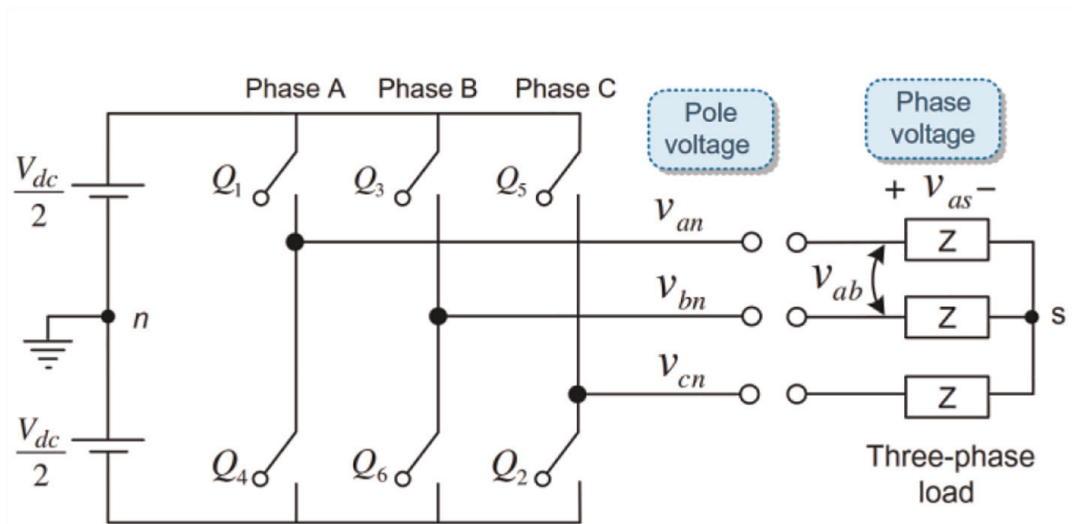


Figure 5.
 Basic configuration of the three-phase square wave inverter.

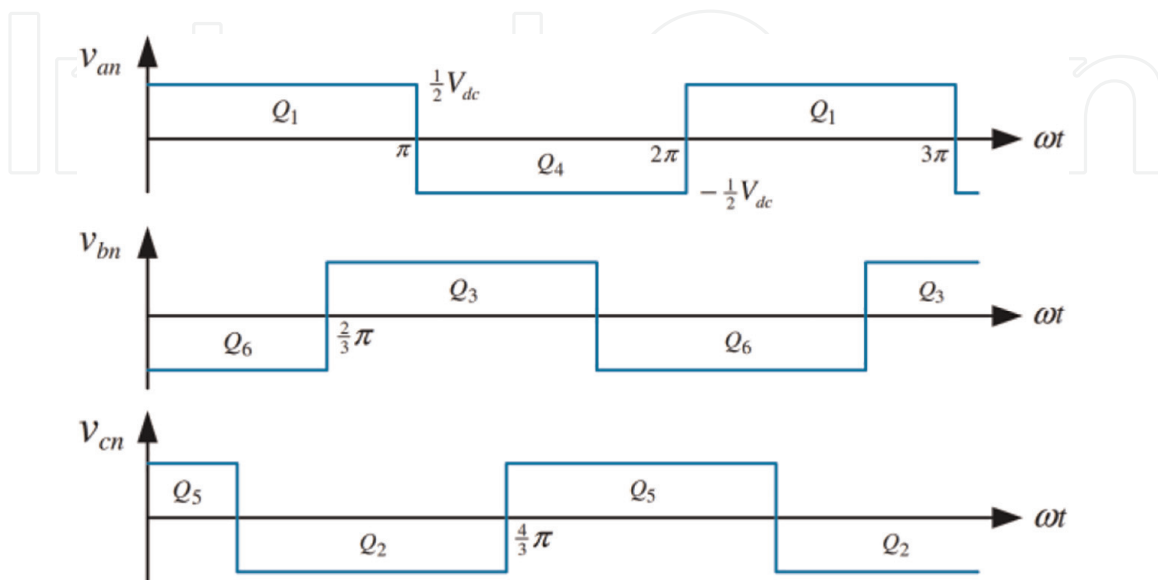


Figure 6.
 Three-phase voltages of the three-phase square wave inverter.

damping to prevent resonance The maximum ripple current I_{max} can be calculated with Eq. (15). In this equation, it is assumed that the maximum peak-to-peak current happens at the inverter modulation factor ($m = 0.5$). Using Eq. (16), the maximum ripple is set to be 10% of the maximum current [40, 41].

$$I_{max} = \frac{P_n \sqrt{2}}{3V_{ph}} \quad (13)$$

$$\Delta I_{Lmax} = 0.1I_{max} \quad (14)$$

With this information, the inverter side inductance L_1 , the grid side inductance L_2 , and the capacitance C_f can be calculated by using Eqs. (17), (18), and (19). The capacitors can be connected either in Δ or Y configuration. The equations below are for Y connection, while for Δ connection the resulting value from Eq. (19) is divided by 3 and the same goes for the damping resistor g_f [37].

$$L_1 = \frac{V_{dc}}{6f_{sw} \Delta I_{Lmax}} \quad (15)$$

$$L_2 = \frac{\sqrt{\frac{1}{k_a^2} + 1}}{C_f f_{sw}^2} \quad (16)$$

$$C_f = x \cdot C_b \quad (17)$$

where k_a is the attenuation factor, and x is the maximum power factor variation as seen by the grid. Next, the resonant frequency and damping resistor can be calculated by using Eqs. (20), (21) [40, 41].

$$\omega_{res} = \sqrt{\frac{L_1 + L_2}{L_1 L_2 C_f}} \quad (18)$$

$$R_f = \frac{1}{3\omega_{res} C_f} \quad (19)$$

It is important that the resonant frequency is kept between the limits in Eq. (22) [40, 41].

$$10f_g < f_{res} < 0.5f_{sw} \quad (20)$$

All the parameters that have been used for the model can be seen in **Table 1**.

2.2 Wind farm

The wind farm consists of a synchronous machine, which is driven by a wind turbine coupled with a diode rectifier and a boost converter that is used to increase the DC-link voltage. A full-bridge inverter is then used to convert the DC power back to three-phase AC. After that, an LCL filter is employed to remove harmonics and smooth out the square waves coming from the inverter. The model is drawn from the MATLAB-Simulink Simscape/special power systems package, where the parameters are designed to satisfy the microgrid requirements [42].

f_g	Grid Frequency	50 Hz
f_{sw}	Switching Frequency	10 kHz
P_n	Nominal Power	60 kW
V_g	Phase Grid Voltage	230 V
V_{dc}	DC-Link Voltage	700 V
x	Maximum Power Variation	20%
k_α	Attenuation Factor	20%
L_1	Inverter Side Inductor	1.4 mH
L_2	Grid Side Inductor	0.374 mH
C_f	Capacitor Filter	160 μ F
R_f	Damping Resistor	0.4528

Table 1.
 Parameter for the LCL filter.

2.2.1 Wind turbine

The wind turbine is modeled using the wind speed V_w , the pitch angle β , and the rotor speed ω_t as input parameters. The equations used for modeling the wind turbine are shown below in Eqs. (23), and the Simulink block model is shown in **Figure 7**. The mechanical system is based on the equation of motion that is displayed in Eq. (24) [43].

$$P_m = \frac{1}{2} \rho A v_w^3 C_p(\lambda, \beta) \quad (21)$$

$$T_{mech} - T_{elec} = I \frac{d\omega}{dt} \quad (22)$$

2.2.2 Synchronous machine

The synchronous machine model has been taken from the specialized power system library and represents the dynamics of the stator, field, and damper windings. It is modeled in the dq -reference frame and is based on Eqs. (25)–(33) [6, 44].

$$V_d = -i_d R_s - \omega \psi_q + \frac{d\psi_d}{dt} \quad (23)$$

$$V_q = -i_q R_s - \omega \psi_d + \frac{d\psi_q}{dt} \quad (24)$$

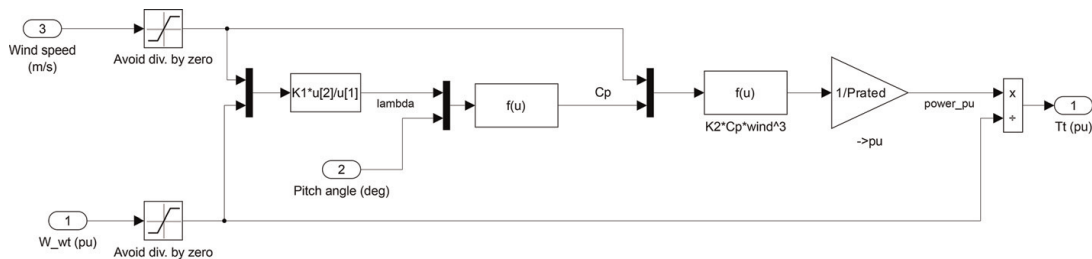


Figure 7.
 The MATLAB-Simulink block model of a wind turbine.

$$V_0 = -i_0 R_0 + \frac{d\psi_0}{dt} \quad (25)$$

$$V_{fd} = V_{fd} = \frac{d\psi_{fd}}{dt} + r_{fd} i_{fd} \quad (26)$$

$$\frac{d\psi_{kd}}{dt} + R_{kd} i_{kd} = 0 \quad (27)$$

$$\frac{d\psi_{kq1}}{dt} + R_{kq1} i_{kq1} = 0 \quad (28)$$

$$\frac{d\psi_{kq2}}{dt} + R_{kq2} i_{kq2} = 0 \quad (29)$$

$$\begin{bmatrix} \psi_d \\ \psi_{kd} \\ \psi_{fd} \end{bmatrix} = \begin{bmatrix} L_{md} + L_f & L_{md} & L_{md} \\ L_{md} & L_{lkd} + L_{f1d} + L_{md} & L_{f1d} + L_{md} \\ L_{md} & L_{f1d} + L_{md} & L_{fd} + L_{f1d} + L_{md} \end{bmatrix} \begin{bmatrix} -i_d \\ i_{kq1} \\ i_{kq2} \end{bmatrix} \quad (30)$$

$$\begin{bmatrix} \psi_q \\ \psi_{kq1} \\ \psi_{kq2} \end{bmatrix} = \begin{bmatrix} L_{mq} + L_f & L_{mq} & L_{mq} \\ L_{mq} & L_{mq} + L_{kq1} & L_{mq} \\ L_{mq} & L_{mq} & L_{mq} + L_{kq2} \end{bmatrix} \begin{bmatrix} -i_d \\ i_{kd} \\ i_{fd} \end{bmatrix} \quad (31)$$

All the nomenclatures of the parameters in the equations can be found in [44].

2.2.3 Back-to-Back boost converter

A library from MathWorks' current collection was also used to select the back-to-back boost converter. It is a part of the library's specialized power systems block for wind turbine subsystems. **Figure 8** depicts the model. Three-phase AC from the synchronous machine is fed into the back-to-back boost converters, which are then transformed into DC by a diode bridge (rectifier). The voltage is subsequently increased by the boost converter; for further information on the boost converter, see Section 2.1.1. The three-phase square wave inverter, which is discussed in Section 2.1.3, is then given the stepped-up DC voltage.

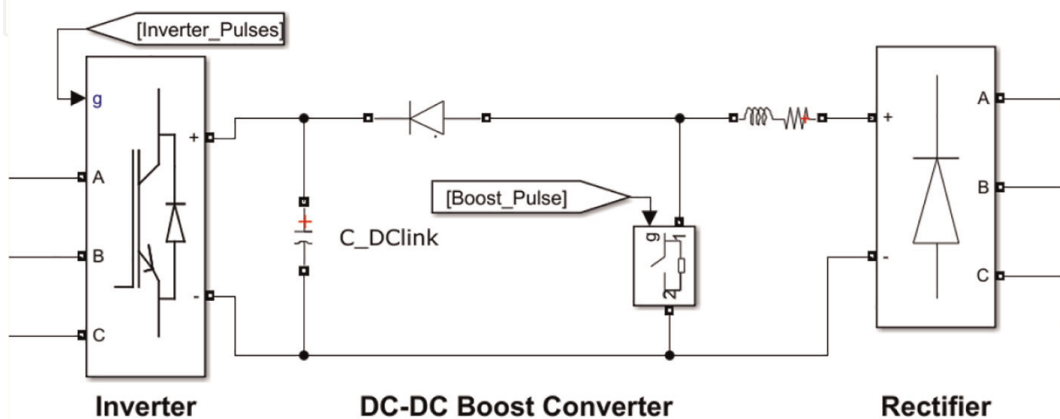


Figure 8. The MATLAB-Simulink model of the back-to-back converter with DC-DC boost converter in DC-link.

2.3 Energy storage system

It is crucial to have the ability to store energy during periods of high-power generation and use it during periods of low generation since the renewable energy sources in the microgrid are very intermittent and dependent on the environment. Additionally, the ESS (Energy Storage System) can be utilized to peak-shave, trade with the grid, and enhance the microgrid's dependability and power quality. It is made up of an L-filter, a three-phase square wave inverter, and a lithium-ion battery bank as illustrated in **Figure 9**. The Simulink model of the ESS is displayed in **Figure 10**.

2.4 Lithium-ion battery

Eq. (34) describes the discharging process of the lithium-ion battery, while Eq. (35) describes the charging process of the battery [28].

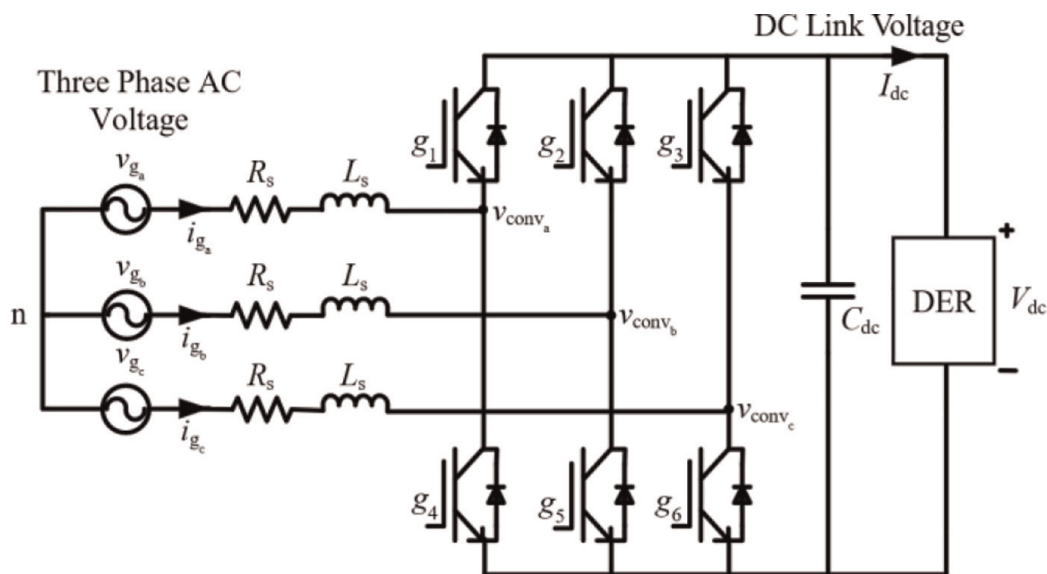


Figure 9.
 Circuit diagram of the bidirectional grid converter.

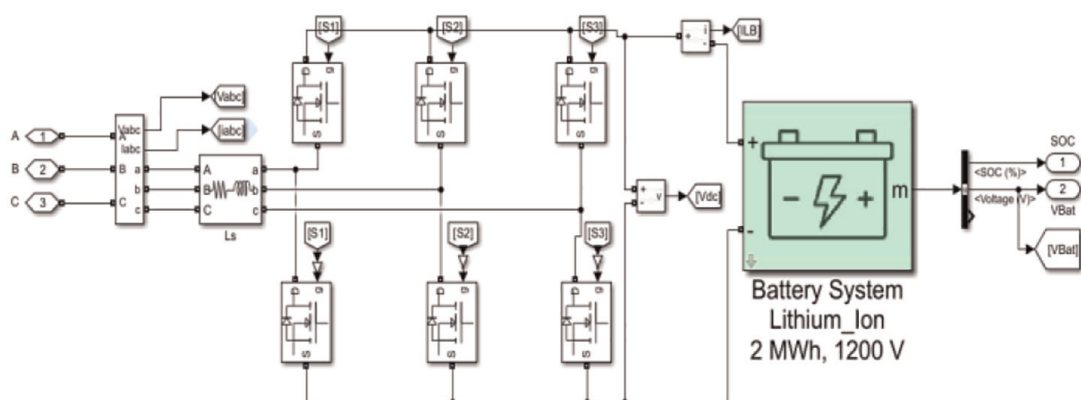


Figure 10.
 The MATLAB-Simulink model of the battery storage system.

$$f_1(it, i^*, i) = E_0 - K \frac{Q}{Q - it} i^* - K \frac{Q}{Q - it} it + Ae^{-B.it} \quad (32)$$

$$f_2(it, i^*, i) = E_0 - K \frac{Q}{it + 0.1Q} i^* - K \frac{Q}{Q - it} it + Ae^{-B.it} \quad (33)$$

Where E_0 is the constant voltage, K is the polarization constant (V/Ah), i^* is the low- frequency current dynamics, i is the battery current, it is the extracted capacity in Ah, Q is the maximum battery capacity, A is the exponential voltage, and B is the exponential capacity (**Figure 11**).

2.5 Hydrogen fuel cell

The backup power source is present so that the microgrid can continue to operate in islanded mode even when the energy storage system's state of charge (SOC) is low. The backup power source in this microgrid is a hydrogen fuel cell. The fuel cell is modeled as a dependent voltage source with a series internal resistance and internal diode as displayed in the equivalent electric circuit as depicted in **Figure 12**. The inverter used with the fuel cell is the same as the one used with the battery illustrated in **Figure 9** and it also uses the same control architecture.

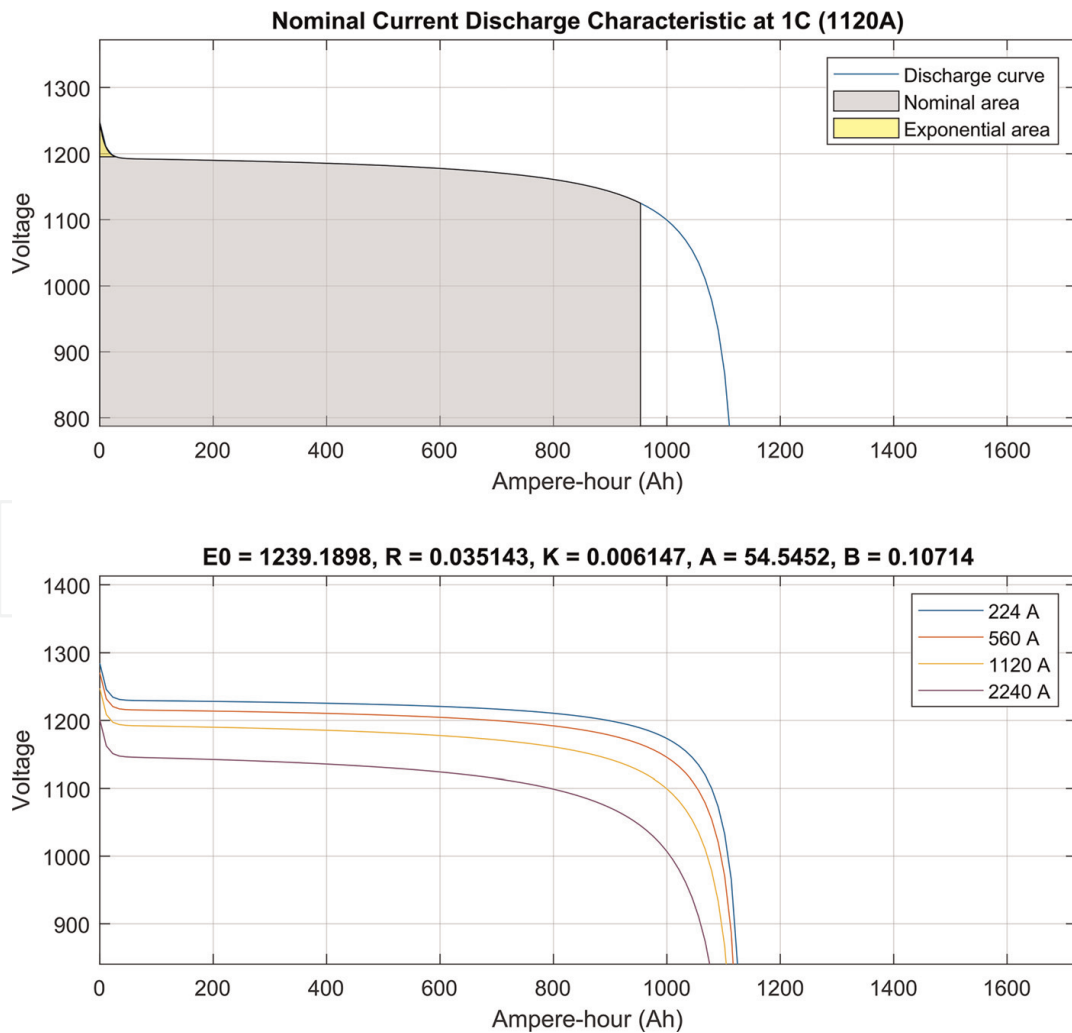


Figure 11. Discharge characteristics of the battery storage model at different currents.

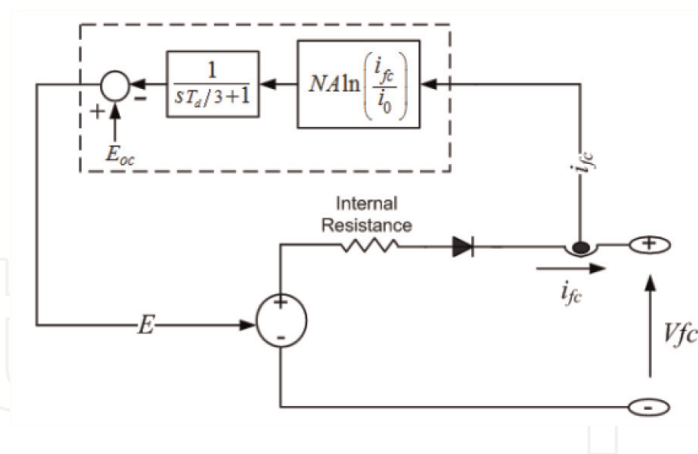


Figure 12.
 Equivalent circuit diagram of the fuel cell.

3. Development and testing of an energy management system (EMS) algorithm

3.1 The proposed EMS algorithm

The suggested approach for controlling the energy flow is depicted in a flowchart in **Figure 13**. The suggested EMS additionally considers the battery limitations, which state that the battery should never be charged below or above the limits (SOC), nor should the maximum charging or discharging current, denoted by $P_{bat,max}$, be exceeded. The algorithm was created using a MATLAB function. Following the validation of the SOC restrictions, the algorithm checks to see if the microgrid is generating more energy than the load is using; if so, the battery is charged in accordance with the restrictions. If the generation is lower than the load, the battery must discharge, or if the SOC is low, the fuel cell must be engaged.

3.2 Testing scenarios and results

A number of scenarios were developed to test the effectiveness and dependability of the suggested EMS in the islanded mode. The results are presented in **Figures 14** and **15**, and a summary of these situations is provided in the **Table 2**. Initially, the load reference were set to 10 kW, and the wind and PV reference were increased to generate the full power. This creates an unbalance as the generation is much larger than the load and since the battery can only absorb 50 kW, the generated power had to be limited to by disabling the MPPT and reducing the PV power reference. That is exactly what the EMS did as it can be seen that the MPPT was disabled shortly after 0 and the PV power was limited while making sure that the battery is charging with a maximum power of 50 kW and the load is kept stable at 10 kW. Next, a step in the load active power reference was applied from 10 to 50 kW and at the same instant, a step in the reactive power was also applied from 0 to 44 kVAR, making the load power factor 0.75 lagging. The controller responds appropriately by increasing the PV power reference to meet the load demand while keeping the battery charging at 50 kW. The reactive power demand is also met by the battery controller. After that, a step in the load reactive power was applied from 44 to -44 kVAR which changes the power factor from lagging to leading and the battery also was able to absorb the reactive

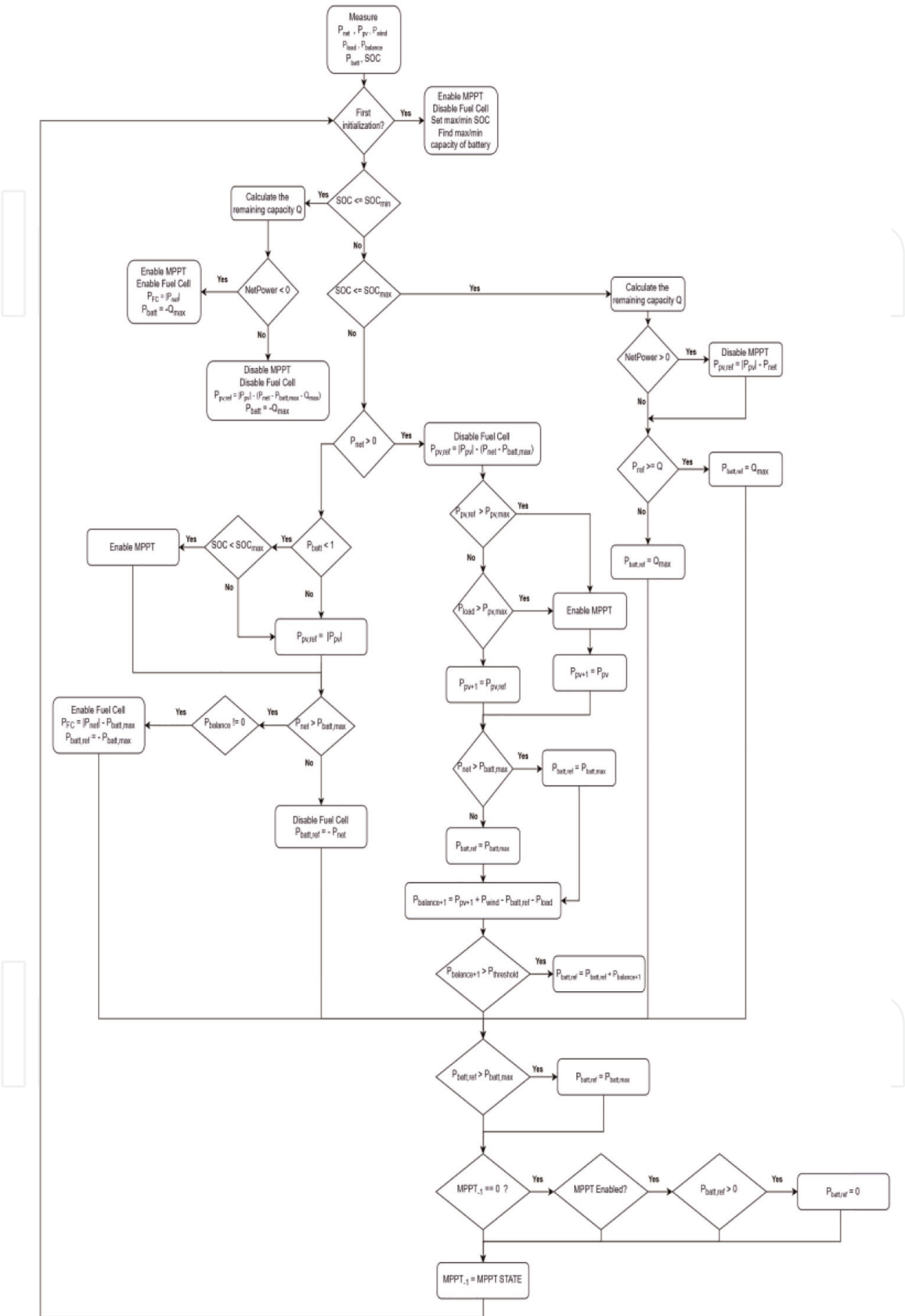


Figure 13.
Flow-chart block diagram of the EMS algorithm.

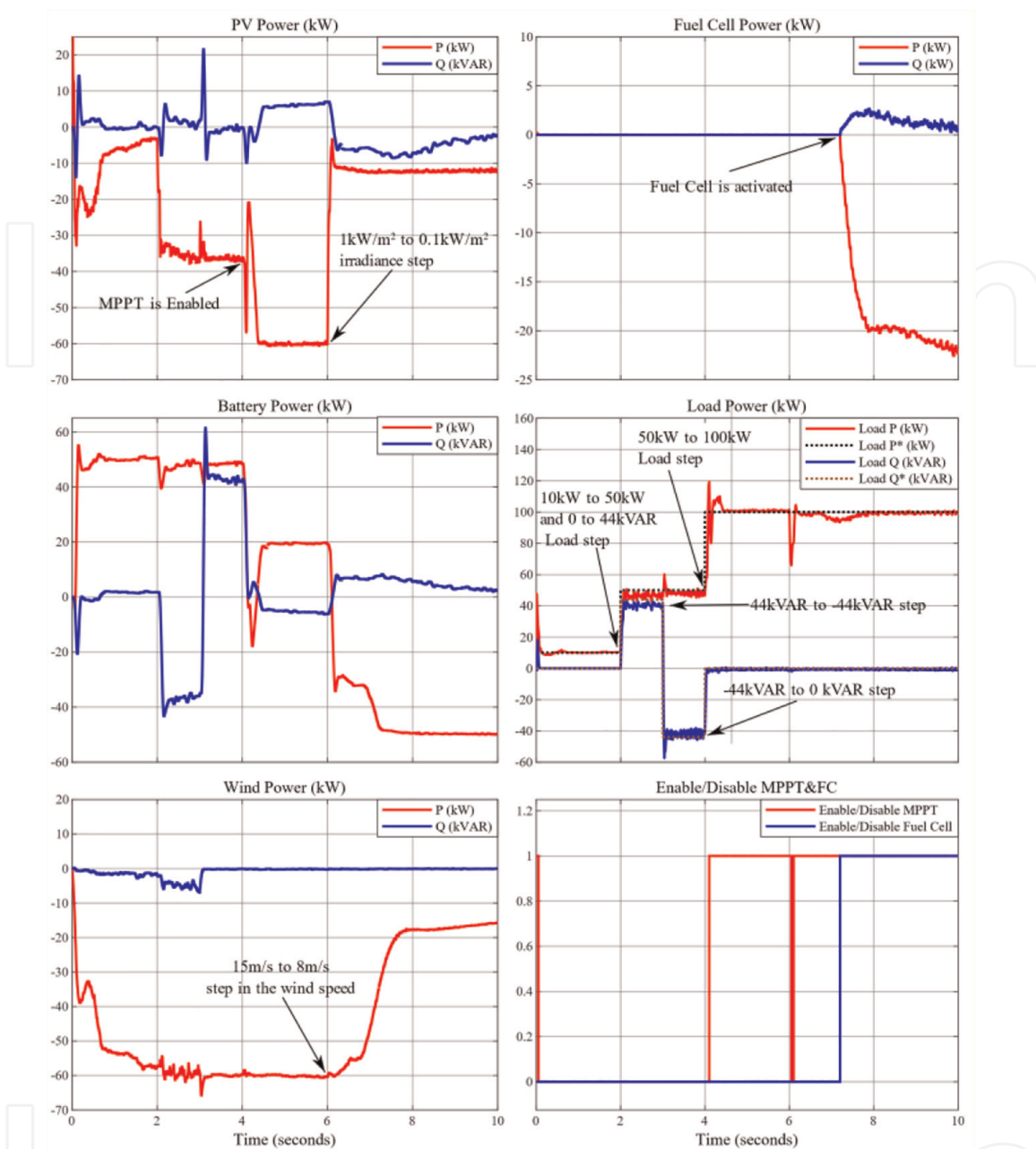


Figure 14. Active and reactive power of different components in the microgrid under loads steps.

power without any issues. At 4 seconds, the reactive power was reset to 0 and another step in the active power was applied from 50 to 100 kW to test the system at full load. Since the load is now much higher, the EMS enabled the MPPT to ensure taking the maximum power of 60 kW available from the PV. The remaining power came from the wind and any excess power was used to charge the battery. Finally, at 6 seconds, the generation was reduced even further to test the scenario where the load is higher than the generation. A step in the irradiance from 1000 to 100 W/m² was applied to the PV and a similar step in the wind speed was applied from 15 to 8 m/s. As the wind power generation was gradually reducing, the EMS sent control commands to the battery to supply the remaining power and the battery started discharging up to

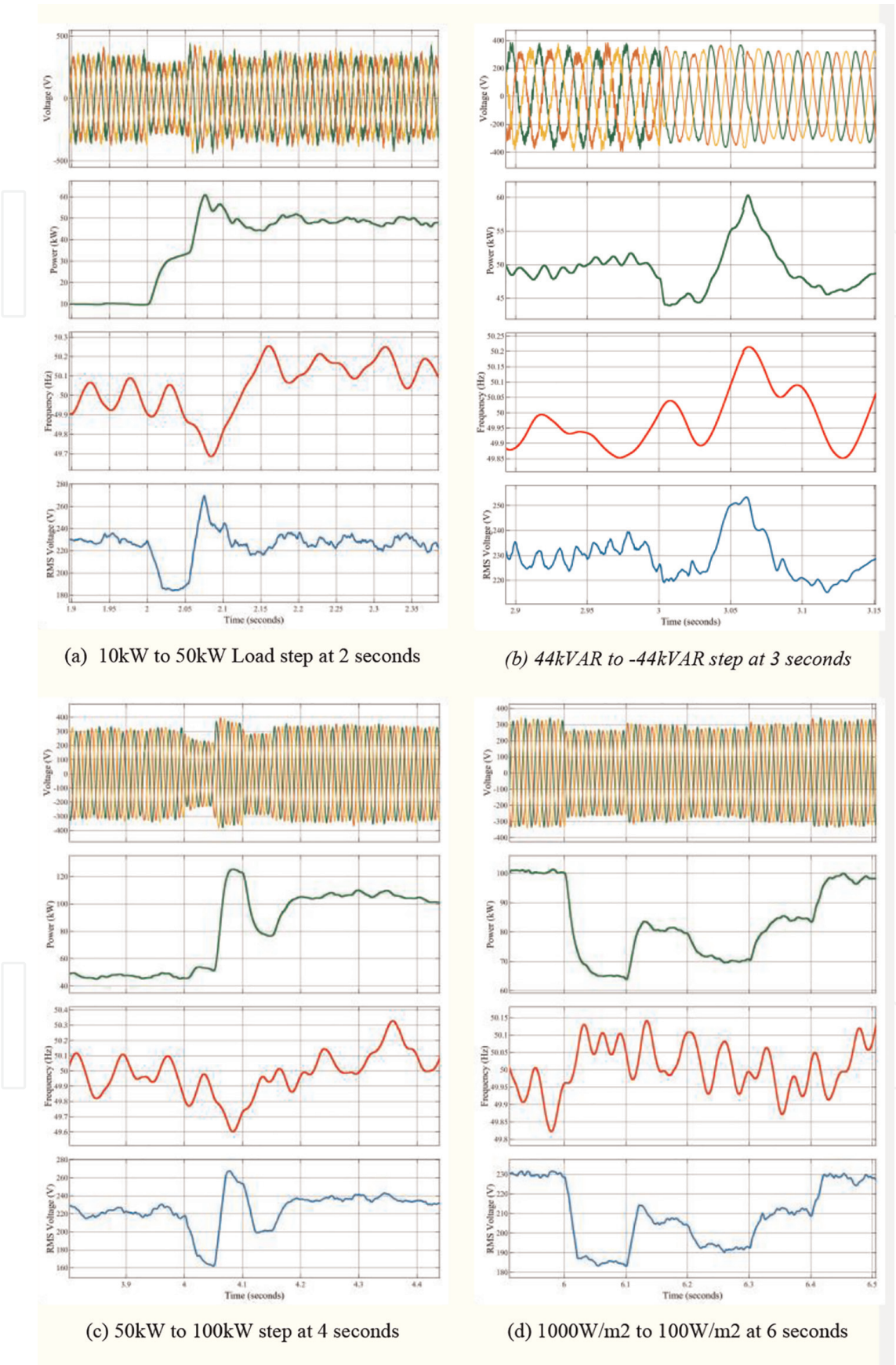


Figure 15. Three-phase voltage, power, frequency, and RMS value of the load under different scenarios. (a) 10 to 50 kW load step at 2 seconds. (b) 44 to -44 kVAR step at 3 seconds. (c) 50 to 100 kW step at 4 seconds. (d) 1000 to 100 W/m² at 6 seconds.

Scenario Time	Description
At 2 seconds	Step change in the active power reference from 10 to 50 kW and in the reactive power from 0 to 44 kVAR
At 3 seconds	Step change in the reactive power reference from 44 to -44 kVAR
At 4 seconds	Step change in the active power reference from 50 to 100 kW and in
At 6 seconds	Step change in the irradiance from 1000 to 100 W/m ² and in the

Table 2.
 Summary of the scenarios tested with energy management system in islanded.

-50 kW, once the battery reached its maximum discharging power, the fuel cell had to be enabled to supply the remaining load power and that is what happened at around 7 seconds. From there on, all the microgrid sources were working in tandem to keep the load power at 100 kW while the EMS adjusted the fuel cell reference based on the power generated by the wind and PV system. These scenarios clearly illustrate that the proposed energy management system is robust and can successfully control the microgrid under various conditions.

The wind and solar references were initially maximized to produce the maximum electricity with the load reference set at 10 kW. Due to the imbalance caused by the generation being significantly greater than the load and the battery's ability to store only 50 kW of power, the generated power has to be constrained by turning off the MPPT and lowering the PV power reference. The MPPT was disabled shortly after zero, and the PV power was limited to ensure that the battery was charging with a maximum power of 50 kW and the load was maintained at 10 kW. This is exactly what the EMS performed.

The load's active power reference was then increased from 10 to 50 kW, and at the same time, the load's reactive power was increased from 0 to 44 kVAR, resulting in a load power factor of 0.75 lagging. In order to fulfill the load requirement, the controller increases the PV power reference as necessary, keeping the battery charging at 50 kW. The battery controller also satisfies the demand for reactive power. The power factor was then changed from lagging to leading by applying a step in the reactive power of the load from 44 to -44 kVAR, and the battery was able to absorb the reactive power without any problems.

To test the system at maximum load, the reactive power was reset to 0 at 4 seconds and another step in the active power was applied from 50 to 100 kW. Due to the increased load, the MPPT was enabled to use the full 60 kW of available PV power thanks to the EMS. Wind provided the remaining energy, and any extra was used to recharge the batteries. To test the condition where the demand is more than the generation, the generation was further decreased at 6 seconds. The PV received a step-down in irradiance from 1000 to 100 W/m² and a comparable step-down in wind speed from 15 to 8 m/s.

The fuel cell had to be enabled in order to supply the remaining load power, which occurred at roughly 7 seconds as the wind power generation rapidly decreased. The EMS had issued control commands to the battery to deliver the remaining power, and the battery began depleting up to -50 kW. The EMS controlled the fuel cell reference depending on the electricity produced by the wind and PV systems, all the microgrid sources continued to cooperate to maintain the load power at 100 kW. These examples unmistakably show how reliable the energy management system is and how successfully it can operate the microgrid under diverse circumstances.

Following that, the battery's SOC constraints were evaluated using the scenarios depicted in **Figure 16**. **Figure 17(a)** shows a zoomed-in plot of the voltage, frequency,

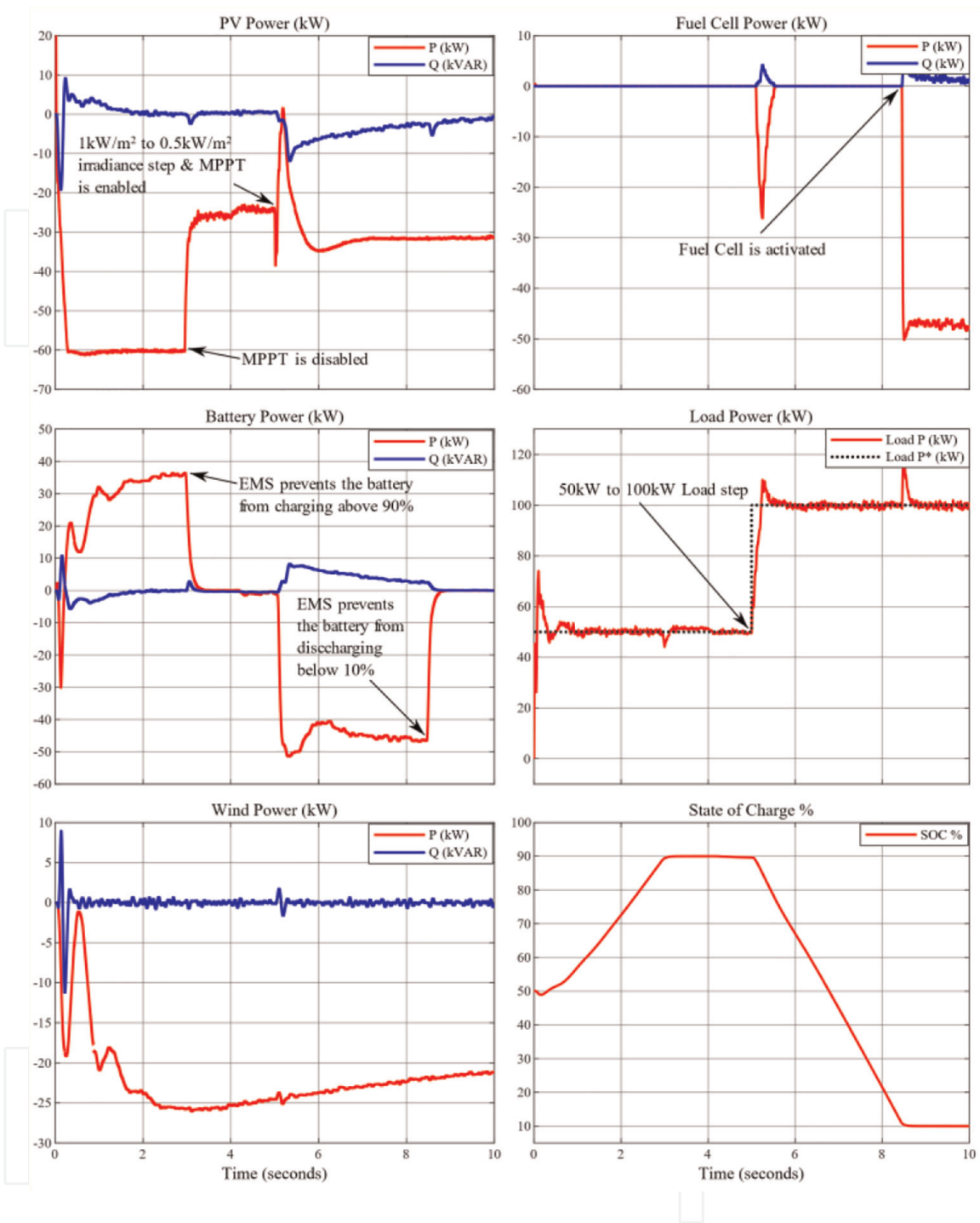


Figure 16. Active and reactive power of different components in the microgrid to test SOC limiting to protect the battery.

and load consumption at 3 seconds when the controller determined the SOC to be above the limits at 3 s, the battery immediately stopped charging, and the PV could no longer operate at the maximum power point and was given a corresponding reference so the power balance in the microgrid was met. The load is increased to 100 kW at 5 seconds, and the PV irradiance is decreased to 500 W/m². To accommodate the significant increase in load demand, this should cause the battery to begin discharging.

After 8 seconds, the battery starts to deplete until it hits 10%, at which point the EMS sends a command to stop discharging the battery. When this occurs, the EMS responds by igniting the fuel cell to start supplying power right away. In

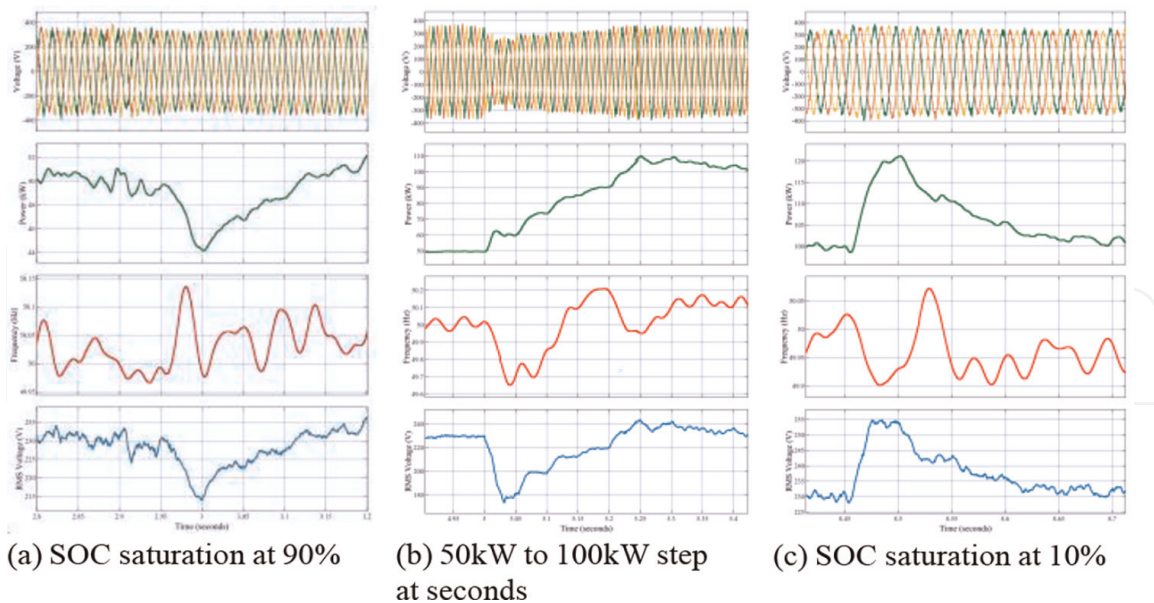


Figure 17. Three-phase voltage, power, frequency, and RMS value of the load under different scenarios. (a) SOC saturation at 90%. (b) 50 to 100 kW step at seconds. (c) SOC saturation at 10%.

Figure 17(c) the voltage, frequency, and load consumption charts are zoomed in. This demonstrates how the EMS can safeguard the battery from overcharging and over-discharging, demonstrating how it accomplishes some of the goals of a BMS (Battery Management System).

4. Conclusion

In summary, this chapter explored the modeling and simulation of microgrid components, including PV system, wind turbine system, battery storage and fuel cell system. The control architecture, developed for the primary control of these components, was based on model predictive control. An energy management system algorithm was successfully designed and developed to control the power flow and to ensure continuous power delivery to the load under all circumstances. The algorithm was tested on a variety of scenarios and proved its robustness and flexibility. When the generation exceeds the load demand and the battery cannot absorb all the excess power, the EMS would disable the MPPT to limit the generation from the solar cell to protect the battery. If the load demand exceeds the generation, the EMS uses the battery to make up for the difference and if the battery power is not sufficient, the fuel cell is activated to provide the rest of the power. Moreover, SOC- based protection scheme was also implemented to ensure that the battery state of charge remains within acceptable limits which increase the lifetime of the battery.

5. Future work

The simulation of the EMS algorithm presented in this paper provides a promising proof- of-concept for its effectiveness in managing electrical energy in a microgrid. However, there are several avenues for further exploration and improvement. One

important step for the validation of the EMS algorithm would be to test it on real hardware, such as a Hardware-in-the-Loop (HIL) platform. This would enable us to evaluate the algorithm's performance in a realistic setting, which includes the various noise and uncertainties that can arise in the physical world. Moreover, we could measure the real-time performance of the algorithm and compare it with the simulation results.

Another potential area for future work is to add new equipment to the microgrid and reconfigure the algorithm accordingly. The EMS algorithm was designed to work with a specific set of components, and its performance may be affected by the addition or removal of equipment. Hence, future expansion of the microgrid may require a readjustment of the algorithm to ensure its optimal operation.

Finally, the implementation of the EMS algorithm presented in this paper was focused on a single microgrid. However, in practice, multiple microgrids can be interconnected to form a larger network, and the EMS algorithm must be adapted to this scenario. Future work could explore the development of a hierarchical control scheme that manages multiple microgrids simultaneously.

Funding

This research was partial funded by the EEA and Norway grant/project DOITSMARTER, contract no 2022/337335.

Conflict of interest


The authors declare no conflict of interest.

Author details

Andreas Pedersen, Ibrahim Ahmed and Lucian Mihet-Popa*
Faculty of Information Technology, Engineering and Economics, Østfold University College, Fredrikstad, Norway

*Address all correspondence to: lucian.mihet@hiof.no

IntechOpen

© 2023 The Author(s). Licensee IntechOpen. This chapter is distributed under the terms of the Creative Commons Attribution License (<http://creativecommons.org/licenses/by/3.0>), which permits unrestricted use, distribution, and reproduction in any medium, provided the original work is properly cited. 

References

- [1] Chandorkar MC, Divan DM, Adapa R. Control of parallel connected inverters in standalone AC supply systems. *IEEE Transactions on Industry Applications*. 1993;**29**(1):136-143
- [2] IEEE-SA Standards Board. *IEEE Standard for Interconnecting Distributed Resources with Electric Power Systems*. New York, United States: IEEE; 2003. pp. 1-28
- [3] Nicholas JJS-G, Miller W, Price WW. Dynamic modeling of GE 1.5 and 3.6 wind turbine-generators. In: 2003 IEEE Power Engineering Society General Meeting (IEEE Cat. No.03CH37491). Vol. 3. Toronto, ON, Canada: IEEE; 2003. pp. 1977-1983. DOI: 10.1109/PES.2003.1267470
- [4] Blaabjerg F, Teodorescu R, Liserre M, Timbus AV. Overview of control and grid synchronization for distributed power generation systems. *IEEE Transactions on Industrial Electronics*. 2006;**53**(5):1398-1409
- [5] Lopes JAP, Moreira CL, Madureira AG. Defining control strategies for microgrids islanded operation. *IEEE Transactions on Power Apparatus and Systems*. 2006;**21**(2): 916-924
- [6] Kundur P. *Power System Stability & Control*. 2nd ed. New York, United States: McGraw Hill; 2022
- [7] Hasaneen BM, Mohammed AAE. Design and simulation of DC/DC boost converter. In: 2008 12th Int. Middle East Power Syst. Conf. MEPCON. Vol: 2008. Aswan, Egypt: IEEE; 2008. pp. 335-340
- [8] Guerrero JM, Vasquez JC, Matas J, De Vicuña LG, Castilla M. Hierarchical control of droop-controlled AC and DC microgrids—A general approach toward standardization. *IEEE Transactions on Industrial Electronics*. 2010;**58**(1): 158-172
- [9] Cho C, Jeon J-H, Kim J-Y, Kwon S, Park K, Kim S. Active synchronizing control of a microgrid. *IEEE Transactions on Power Electronics*. 2011;**26**(12):3707-3719
- [10] Cortes P, Rodriguez J, Silva C, Flores A. Delay compensation in model predictive current control of a three-phase inverter. *IEEE Transactions on Industrial Electronics*. 2011;**59**(2): 1323-1325
- [11] Lidula NWA, Rajapakse AD. Microgrids research: A review of experimental microgrids and test systems. *Renewable and Sustainable Energy Reviews*. 2011;**15**(1):186-202
- [12] Marnay C, DeForest N, Lai J. A green prison: The Santa Rita jail campus microgrid. In: 2012 IEEE Power and Energy Society General Meeting. San Diego, CA, USA: IEEE; 2012. pp. 1-2
- [13] Rocabert J, Luna A, Blaabjerg F, Rodriguez P. Control of power converters in AC microgrids. *IEEE Transactions on Power Electronics*. 2012;**27**(11):4734-4749
- [14] Yang H, Li Q, Chen W. Microgrid communication system and its application in hierarchical control. In: *Smart Power Distribution Systems: Control, Communication, and Optimization*. Basel, Switzerland: MDPI, Academic Press; 2019. pp. 179-204
- [15] Vasquez JC, Guerrero JM, Savaghebi M, Eloy-Garcia J, Teodorescu R. Modeling, analysis, and design of stationary-reference-frame

- droop-controlled parallel three-phase voltage source inverters. IEEE Transactions on Industrial Electronics. 2012;**60**(4):1271-1280
- [16] Hirose K, Reilly J, Irie H. The Sendai microgrid operational experience in the aftermath of the tohoku earthquake: A case study. New Energy & Industrial Technology Development Organization. 2013;**308**:1-6
- [17] Hu J, Zhu J, Dorrell DG. Generation, and undefined 2014. "Model Predictive Control of Inverters for both Islanded and Grid-Connected Operations in Renewable Power Generations". Vol. 8 (3). New York, United States: Wiley Online Library; 2013. pp. 240–248
- [18] Fotopoulou MC, Drosatos P, Petridis S, Rakopoulos D, Stergiopoulos F, Nikolopoulos N. Model predictive control for the energy Management in a District of buildings equipped with building integrated photovoltaic systems and batteries. Energies. 2021;**14**(12): 3369
- [19] Dehghanzadeh A, Farahani G, Vahedi H, Al-Haddad K. Model predictive control design for DC-DC converters applied to a photovoltaic system. Electrical Power and Energy Systems. 2018;**103**:537-544
- [20] Metry M, Balog RS. An adaptive model predictive controller for current Sensorless MPPT in PV systems. IEEE Open Journal of Power Electronics. 2020;**1**:445-455. DOI: 10.1109/OJPEL.2020.3026775
- [21] Zhao Y, An A, Xu Y, Wang Q, Wang M. Model predictive control of grid-connected PV power generation system considering optimal MPPT control of PV modules. Protection and Control of Modern Power Systems. 2021;**6**:32. DOI: 10.1186/s41601-021-00210-1
- [22] Lashab A, Sera D, Guerrero J, Mathe L, Bouzid A. Discrete model predictive control-based maximum power point tracking for PV systems: Overview and evaluation. IEEE Transactions on Power Electronics, Institute of Electrical and Electronics Engineers. 2018;**33**(8):7273-7287
- [23] Minchala LI, Zhang Y, Probst O. Design of an Energy Management System for secure integration of renewable energy sources into microgrids. In: Cao W-P, Yang J, editors. Development and Integration of Microgrids. Rijeka: IntechOpen; 2017
- [24] Justo JJ, Mwasilu F, Lee J, Jung J-W. AC-microgrids versus {DC}-microgrids with distributed energy resources: A review. Renewable and Sustainable Energy Reviews. 2013;**24**:387-405
- [25] Mnih V et al. Playing atari with deep reinforcement learning. arXiv Prepr. 2013. pp. 1-9
- [26] Rodriguez J et al. State of the art of finite control set model predictive control in power electronics. IEEE Transactions on Industrial Informatics. 2013;**9**(2):1003-1016
- [27] Shafiee Q, Guerrero JM, Vasquez JC. Distributed secondary control for islanded microgrids—A novel approach. IEEE Transactions on Power Electronics. 2013;**29**(2):1018-1031
- [28] Zhu C, Li X, Song L, Xiang L. Development of a theoretically based thermal model for lithium ion battery pack. Journal of Power Sources. 2013; **223**:155-164
- [29] Hu J, Zhu J, Dorrell DG. Model predictive control of grid- connected

- inverters for PV systems with flexible power regulation and switching frequency reduction. *IEEE Transactions on Industry Applications*. 2014;**51**(1): 587-594
- [30] Olivares DE et al. Trends in microgrid control. *IEEE Transactions on Smart Grid*. 2014;**5**(4):1905-1919
- [31] Ahumada C, Cárdenas R, Saez D, Guerrero JM. Secondary control strategies for frequency restoration in islanded microgrids with consideration of communication delays. *IEEE Transactions on Smart Grid*. 2015;**7**(3): 1430-1441
- [32] Xue C, Zhou D, Li Y. Hybrid model predictive current and voltage control for LCL-filtered grid-connected inverter. *IEEE Journal of Emerging and Selected Topics in Power Electronics*. 2021;**9**(5): 5747-5760
- [33] Silvestre S. Chapter 7 - strategies for fault detection and diagnosis of PV systems. In: Yahyaoui I, editor. *Advances in Renewable Energies and Power Technologies*. Amsterdam, Netherlands: Elsevier; 2018. pp. 231-255
- [34] Ram JP, Manghani H, Pillai DS, Babu TS, Miyatake M, Rajasekar N. Analysis on solar PV emulators: A review. *Renewable and Sustainable Energy Reviews*. 2018;**81**:149-160
- [35] Bensalem S, Chegaar M, Herguth A. Band gap dependence with temperature of semiconductors from solar cells electrical parameters. *Current Applied Physics*. 2017;**17**(1):55-59
- [36] Ghani F, Duke M, Carson J. Numerical calculation of series and shunt resistance of a photovoltaic cell using the Lambert W-function: Experimental evaluation. *Solar Energy*. 2013;**87**(1):246-253
- [37] Chee WT, Green TC, Carlos AHA. Analysis of perturb and observe maximum power point tracking algorithm for photovoltaic applications. In: *PECon 2008 - 2008 IEEE 2nd Int. Power Energy Conf. Johor Bahru, Malaysia: IEEE; 2008. pp. 237-242*
- [38] Lee BK, Ehsani M. A simplified functional simulation model for three-phase voltage-source inverter using switching function concept. *IEEE Transactions on Industrial Electronics*. 2001;**48**(2):309-321
- [39] Liserre M, Teodorescu R, Rodriguez P. Photovoltaic inverter structures. In: *Grid Converters for Photovoltaic and Wind Power Systems*. Chichester, United Kingdom: John Wiley and Sons; 2011. pp. 26-29
- [40] Beres RN, Wang X, Liserre M, Blaabjerg F, Bak CL. A review of passive power filters for three-phase grid-connected voltage-source converters. *IEEE Journal of Emerging and Selected Topics in Power Electronics*. 2016;**4**(1): 54-69
- [41] Reznik A, Simões MG, Al-Durra A, Mueen SM. LCL filter design and performance analysis for grid-interconnected systems. *IEEE Transactions on Industry Applications*. 2014;**50**(2):1225-1232
- [42] Ekanayake JB, Holdsworth L, Jenkins N. Comparison of 5th order and 3rd order machine models for doubly fed induction generator (DFIG) wind turbines. *Electric Power Systems Research*. 2003;**67**(3):207-215
- [43] Teodorescu R, Liserre M, Rodríguez P. Grid converters for photovoltaic and wind power systems. *Grid Converters for Photovoltaic and Wind Power Systems*. 2010. pp. 125-144

[44] Moeini A, Kamwa I, Brunelle P, Sybille G. Synchronous machine stability model, an update to IEEE Std 1110-2002 data translation technique. In: 2018 IEEE Power Energy Society General Meeting (PESGM). Portland, OR, USA: IEEE; 2018. pp. 1-5

IntechOpen

IntechOpen